Journal of
Materials Chemistry A

Accepted Manuscript

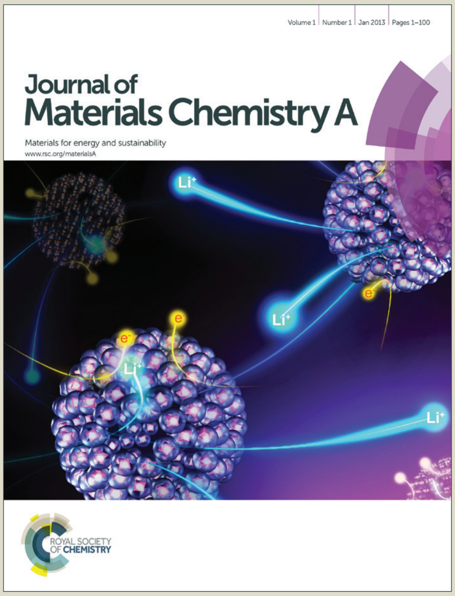

ROYAL SOCIETY
OF CHEMISTRY

www.rsc.org/materialsA

Multiporous nanofibers of SnO_2 by electrospinning for high efficiency dye-sensitized solar cells

Qamar Wali, Azhar Fakharuddin, Irfan Ahmed, Mohd Hasbi Ab Rahim, Jamil Ismail, Rajan Jose*

Nanostructured Renewable Energy Materials Laboratory, Faculty of Industrial Sciences &
Technology, Universiti Malaysia Pahang, 26300, Malaysia
*Corresponding author: rjose@ump.edu.my

Various one-dimensional nano-morphologies such as multiporous nanofibers (MPNFs), porous nanofibers (PNFs), and nanowires (NWs) of SnO_2 are synthesized using electrospinning technique by controlling the tin precursor concentration. The MPNFs have ~ 8 - fold higher surface area compared to the other morphologies. Dye-sensitized solar cells (DSCs) were fabricated using these nanostructures as photoanodes and compared their performance. The MPNFs surpass performance of PNFs and NWs as well as conventional TiO_2 paste. Record photoconversion efficiency (PCE) of ~7.4% is realized in MPNFs DSCs which is twice to that achieved using PNFs (~ 3.5%). Furthermore, the MPNFs showed over >80% incident photon to current conversion efficiency (22% higher than that achieved by spherical P25 TiO_2 particles) and also demonstrated ~3 times longer electron lifetime and electron diffusion length. Owing to the possibility to produce large quantities using electrospinning technique, huge commercial potential of SnO_2 nanostructures, and promising results achieved herewith the MPNFs are expected to soon be utilized in commercial devices.

1 Introduction

Nanostructured materials of novel morphologies are attractive owing to their promising physical and chemical properties exploitable in emerging nanodevices.[1, 2] Primary attention to the nanomaterials is due to their high surface to volume ratio so that a given function can be served using fewer materials than their bulk counterparts. The past two decades have witnessed interesting one-dimensional (1D) nanostructures such as nanowires, nanotubes, nanoforrests, nanofibers, and nanorods due to their anisotropic properties.[3, 4] The hollow nanofibers have two surfaces thereby offering two times higher surface area than the other 1D structures.[5, 6] Among the many techniques for forming 1D morphologies, electrospinning is a simple and versatile technique for producing nanostructures and membranes for many engineering applications including filtration, healthcare, and energy.[7-9] In the electrospinning technique, an organic polymeric solution is spun by an electric field ($\sim 10^5$ Vm^{-1}); resulting solid fibrous mat is collected on a collector surface.[10] Conventional electrospinning process produces random solid fibers; however, immense research during the past decade enabled formation of other morphologies such as tubes,[11, 12] flowers,[13] and rods[8, 14] by controlling the injection strategy or solution chemistry. Electrospun nanowires are proven to be one of the best candidates in almost all areas of science and technology including advanced electronics, renewable energy, environmental, and healthcare.[9]

Tin oxide (SnO_2), an archetypical transparent conducting oxide with larger band gap (~3.6 eV at 300 K),[15] low conduction band effective mass (0.1 m_o),[16] and higher electrical mobility (100-250 $cm^2V^{-1}s^{-1}$)[17] than other metal oxide semiconductors (MOS), is a candidate for many applications such as transparent conducting electrodes, working electrodes for solar cells, batteries, gas sensors, catalyst supports, antireflective coatings, and other optoelectronic devices.[18-20] Considerable efforts have been devoted to develop its nanostructures with diverse morphologies and aspect ratios with an aim to enhance the specific surface area and further improve their properties. Non-conventional morphologies of SnO_2 such as tetrapods[21] and flowers[13] have been synthesized from colloidal solutions with improved properties compared to their particulate or 1D analogues. SnO_2 nanowires and nanotubes are also developed using electrospinning technique with improved properties.[22-24]

However, one of the major limiting factors of these 1D structures is their lower specific surface area which adversely affected the device performance. For example, when these electrospun 1D nanostructures are used as a photoanode of a DSCs, a photovoltaic device in which the photocurrent flows between a dye-anchored nanostructured MOS (n-MOS) and a hole-conducting electrolyte;[25] the lower surface area lead to lower photocurrents (~15%) and inferior photovoltaic performances (24%) than corresponding nanoparticle based DSCs.[26]

The two crucial parameters for improving the performance of SnO_2-based DSCs are (i) improved electronic transport to overcome charge recombination with the electrolyte and (ii) larger surface area to accommodate more dye molecules. Towards the first strategy, Shang *et al*. employed SnO_2 nanorods to improve charge collection and demonstrated photoconversion efficiency (PCE) ~1.2% which is greater than their NPs analogues (0.98%).[26] However, the NRs were of lower surface area (12 m^2/g) compared to NPs (15 m^2/g). Towards the second strategy, a number of reports are recently published on high PCE in DSCs using SnO_2 nanostructures. For example, flower shaped SnO_2 developed by electrospinning resulted in an open circuit voltage (V_{OC}) as high as 700 mV with PCE ~ 3% due to their high surface area (40 m^2/g), larger electron density, and flat band potential compared to nanofibers based DSCs (PCE ~ 0.7%, 19 m^2/g).[13, 17] In another report, Dong *et al.* reported gradual PCE increment in SnO_2 hollow microspheres by increasing number of exterior SnO_2 shells which systematically increased the surface area from ~20 m^2/g to ~39 m^2/g.[27] A final PCE of ~7.2% is reported in a quintuple shell which is ~40% higher than that of a single shell. Although the resulting architecture improved light scattering and enhanced dye-loading, the electronic transport was compromised due to their spherical shape. Therefore, a single morphology employing both of these parameters is actively sought for high efficiency DSCs.

We have now employed the electrospinning procedure and identified conditions for forming nanowires (NWs), porous nanofibers (PNFs), and multiporous nanofibers (MPNFs) of SnO_2 by controlling the precursor concentration. The MPNFs offered 6 – 8 times higher surface area than the PNFs and NWs and gave the highest PCE ~7.4% in SnO_2 based photoelectrodes with appropriate modifications.

2 Experimental

2.1 Synthesis of the SnO_2 nanostructures

The starting materials were tin (iv) chloride pentahydrate ($SnCl_4.5H_2O$), polyvinylpyrrolidone (PVP), dimethylformamide (DMF) and ethanol; all these chemicals were purchased from Sigma Aldrich. As a typical procedure, 3g of PVP were dissolved in an equal volume ratio (1:1) of ethanol and DMF. To this solution, various concentrations of the tin precursor were dissolved at room temperature until the solution become transparent. In brief, the concentrations were 5.5 mM, 7 mM, 8.5 mM, 10 mM, 11.5 mM and are labeled as C_0, C_1, C_2, C_3 and C_4, respectively. The viscosity of the solution for electrospinning was measured with a rheometer (LVDV III Ultra, Brookfield Co., USA).

The solutions were then transferred to plastic syringe with steel needles for electrospinning. The operating parameters were; (i) applied voltage, 25 KV, (ii) the injection rate, 0.6 mLh^{-1}, (iii) distance between the collector and the tip of the needle, 20 cm, (iv) humidity, 40-45%, and (v) the speed of rotating collector, 1200 rpm. Solid nanofibers were then collected from the collector and annealed at temperature 600 ^oC for 3 hour at heating rate 0.5 $^oC\ min^{-1}$.

2.2 Characterizations of nano morphologies

The annealed nanowires were characterized by Crystal structure of the material was studied by X-ray diffraction (XRD) technique using Rigaku Miniflex II X-ray diffractometer employing Cu Kα radiation (λ = 1.5406 Å). Morphology and microstructure of the materials were studied by scanning electron microscopic technique (7800F, FESEM, JEOL, USA). High resolution lattice images and selected area diffraction patterns were obtained using transmission electron microscope (TEM) operating at 300 kV (FEI, Titan 80-300 kV). The BET surface area of the material was measured using gas adsorption studies employing a Micromeritics (Tristar 3000, USA) instrument in the nitrogen atmosphere.

2.3 DSCs Fabrication and measurements

The devices were fabricated as before.[28] In brief, a 500 mg of SnO_2 PNFs and MPNFs were dispersed separately in ethanol and made a translucent suspension. A pre-calculated amount of α-terpinol (α-T) and ethyl cellulose (E.C) were added to it to make 15-18 wt. % respectively in ratio 1:4.1:0.5 (SnO_2:α –T:E.C). A paste was produced as stated elsewhere.[29] This paste was then applied on sequentially pre-cleaned fluorine doped tin oxides (FTOs; ~10 Ω/□) by water, acetone, and ethanol, respectively. A blocking layer was formed on FTOs via $TiCl_4$ treatment for a comparison. The coated FTOs were annealed for 30 min at 450 ^{o}C with the heating rate of 2^{o}C min^{-1}. The FTOs were then taken out and immediately immersed in 0.3 M dye solution of cis-bis(isothiocyanato)bis(2,2'-bipyridyl-4,4'-dicarboxylato)-ruthenium(II)(N3) in absolute ethanol. The dye anchored FTOs were rinsed with ethanol to remove any unanchored dye and dried at room temperature before cell fabrication. The devices were masked using a Suryline spacer (~ 60 µm). The iodide/triiodide redox couple was filled in the gap between the electrodes and pre-heated platinum coated FTO (Solaronix) was used as counter electrode. Hence, SnO_2 PNFs and MPNFs DSCs were fabricated. The active area of the devices was ~0.15 cm^2. A P25 DSCs was also fabricated as a reference cell.

To characterize the morphology and thickness of the films, the as-prepared nanostructures and the coated films were investigated by scanning electron microscopy (FESEM; JEOL-USA). Absorbance spectra of the desorbed electrodes were recorded using a UV-VIS NIR spectrophotometer (UV-2600 SHIMADZU). To investigate the current and voltage of the assembled DSCs, photocurrent measurements were carried out using a solar simulator (SOLAR LIGHT, Model 16-S 150) employing single port simulator with power supply (XPS 400) at 100 mW/cm2. I-V and OCVD measurements curves were obtained using a potentiostat (Autolab PGSTAT30, Eco Chemie B.V., The Netherlands) employing the NOVA® software. The AC responses of the cells were studied using the Autolab PGSTAT30. The impedance spectra were fitted to the well-known transmission line model by Bisquert *et al.*[30] using Z-view software. Both, the real and imaginary parts were simultaneously fitted at absolute temperature 293 K using the "calc-modulus" as "data weighing option". For each type of device at least five sets of devices were fabricated and for MPNFs, the experiment was repeated at least10 times to assure the consistency in the values.

3 Result and discussion3.1 Synthesis and characterization of multiporous nanofibers

The tin precursor concentration in the polymeric solution for electrospinning was varied in five steps from 5.5 mM (C_0) to 11.5 mM (C_4). The as-spun polymeric mats had conventional fiber morphology with similar diameter ~200 – 600 nm (Electronic Supplementary Information, ESI†, Figure S1), which upon annealing resulted in NWs, MPNFs, and PNFs (Fig. 1). Table 1 summarizes the properties of the starting polymeric solutions and morphologies after annealing. Fig. 2 shows FESEM images of annealed nanofibers for samples C_0 (a-c), C_1 (d-f), C_2 (g-i), C_3 (j-l), and C_4 (m-o). For the sample C_0, porous solid NWs were formed with diameter ranging from ~100 – 170 nm. A small increase in the precursor concentration (7 mM, C_1) resulted in the formation of MPNFs with slightly larger diameter (120 – 190 nm); which upon further increments transformed into single channel NTs. The number of channels in MPNFs varied from 2 to 4 with their inner diameters ranging from 30 to 70 nm. Further increase in the precursor concentration (Samples C_2 and C_3) resulted in the formation of PNFs with outer and inner diameters in the range ~160 – 220 and ~50 – 100 nm, respectively. i.e., increase in the precursor concentration in samples C_2 and C_3 resulted in significant decrease in the tube diameter and ultimately the tubes vanished in the sample C_4. For the sample C_4, the over concentration resulted in significantly varying diameter of NWs (210 – 340 nm) which is in accordance with previous report on electrospinning of SnO_2 nanowires.[13]

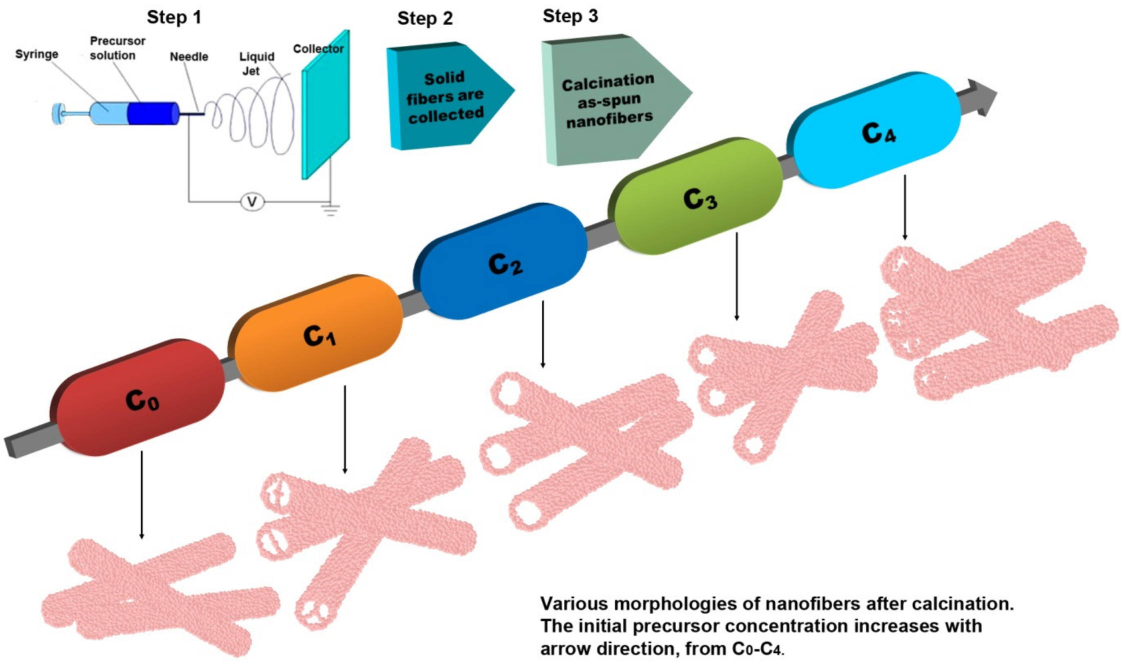

Various morphologies of nanofibers after calcination. The initial precursor concentration increases with arrow direction, from C$_0$-C$_4$.

Fig. 1 Schematic illustration of single and multiporous nanofibers formation.

Table1 Properties of the electrospinning solution and resulting nanostructures after annealing.

Sample label	Precursor Concentration (mM)	Solution Viscosity (cP)	Morphology	Surface area (m^2/g)	Diameter (nm)	Grain size (nm)
C$_0$	5.5	256.7	NWs	7	114-170	18-27
C$_1$	7.0	298.1	MPNFs	78	124-191	5-15
C$_2$	8.5	304.9	PNFs	12	162-224	15-25
C$_3$	10	321.5	PNFs	10	170-195	20-40
C$_4$	11.5	344.2	NWs	10	213-337	30-75

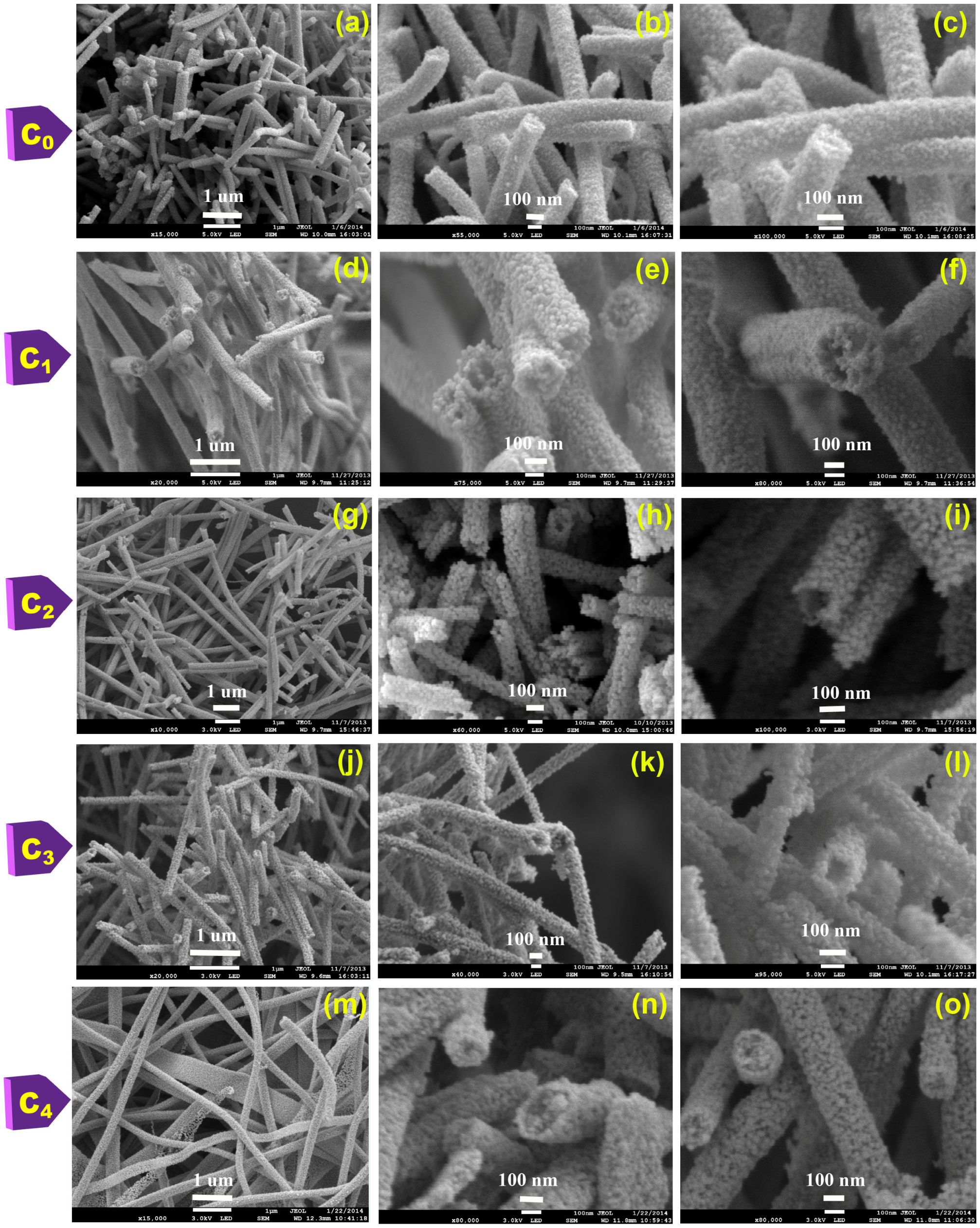

Fig. 2 Field emission scanning electron microscopy (FE–SEM) (a—c) Show C_O NWs, (d—f) depict C_1 MPNFs, (g—i, j—l) demonstrate C_2 and C_3 for PNFs and C_4 (m—o) present the formation of porous nanostructure.

The BET surface area of the samples varied in the 7 – 78 m^2/g with the NWs possess the lowest and MPNFs the highest. The observed 6 – 8 times higher surface area in MPNFs than PNFs is attributed to (i) multichannels inside a single wall and (ii) the smaller grains and pores in MPNFs as confirmed by transmission electron microscopy (TEM) analysis (Fig. 3). In the Fig. 3, the panels (a-b) and (d-e) show TEM images of PNFs and MPNFs, respectively. A highly porous and hollow structure is visible in both cases. The MPNFs were formed with grains of size 5 – 15 nm which are smaller than the grains forming the PNFs (15 – 25 nm). The smaller grains and many channels in MPNFs are therefore the source of its high surface area. The selected area electron diffractions (SAED) (panels c and f in Fig. 3) show concentric circles which are due to polycrystallanity in both nanostructures; however, the PNFs had a relatively spotty pattern. The crystal structures of the samples were verified using X–ray diffraction (XRD); the observed peaks of PNFs and MPNFs from XRD (Fig. 4) pattern are (110), (101), (200) and (211) plans at 26.5°, 34°, 38° and 52° indicate pure SnO_2 nanostructures.[26] Additional crystal planes such as (002) and (321) were observed in MPNFs due to their lower grain size and relatively higher polycrystallinity. The lattice parameters calculated from the observed XRD peaks are a = b = 4.635 Å and c= 3.165 Å which are in close agreement with the standard data (JCPDS Card No 41—1445) of the tetragonal cassiterite structure of space group $P4_2/mnm$. The d-spacing of planes in the HRTEM images are consistent with those in the XRD patterns.

A significant question arise is on the mechanism of formation of variable porosity and the changes in the sizes of the particles composing the fibers with change in concentration of the precursors. As noted before, no change in morphology of the as-prepared fiber either in their cross-section or in the cylindrical surface was observed. To check whether there is any change in crystallinity of the fiber, XRD patterns of the as-spun fibers were measured and presented in ESI† (Figure S2). Inorganic crystalline phases (judged from the sharp peaks) were observed in the as-spun polymeric samples. The crystallographic identify the phases could not be identified; however, the peaks show a reversal of intensity for C_2 (PNFs) compared to C_1 (MPNFs) indicating the change in orientation of the crystallites – which is expected to be the source of variable porosity upon changing the precursor concentration. Nevertheless, a deep investigation of the mechanism on the formation of variable pores will be investigated and presented elsewhere.

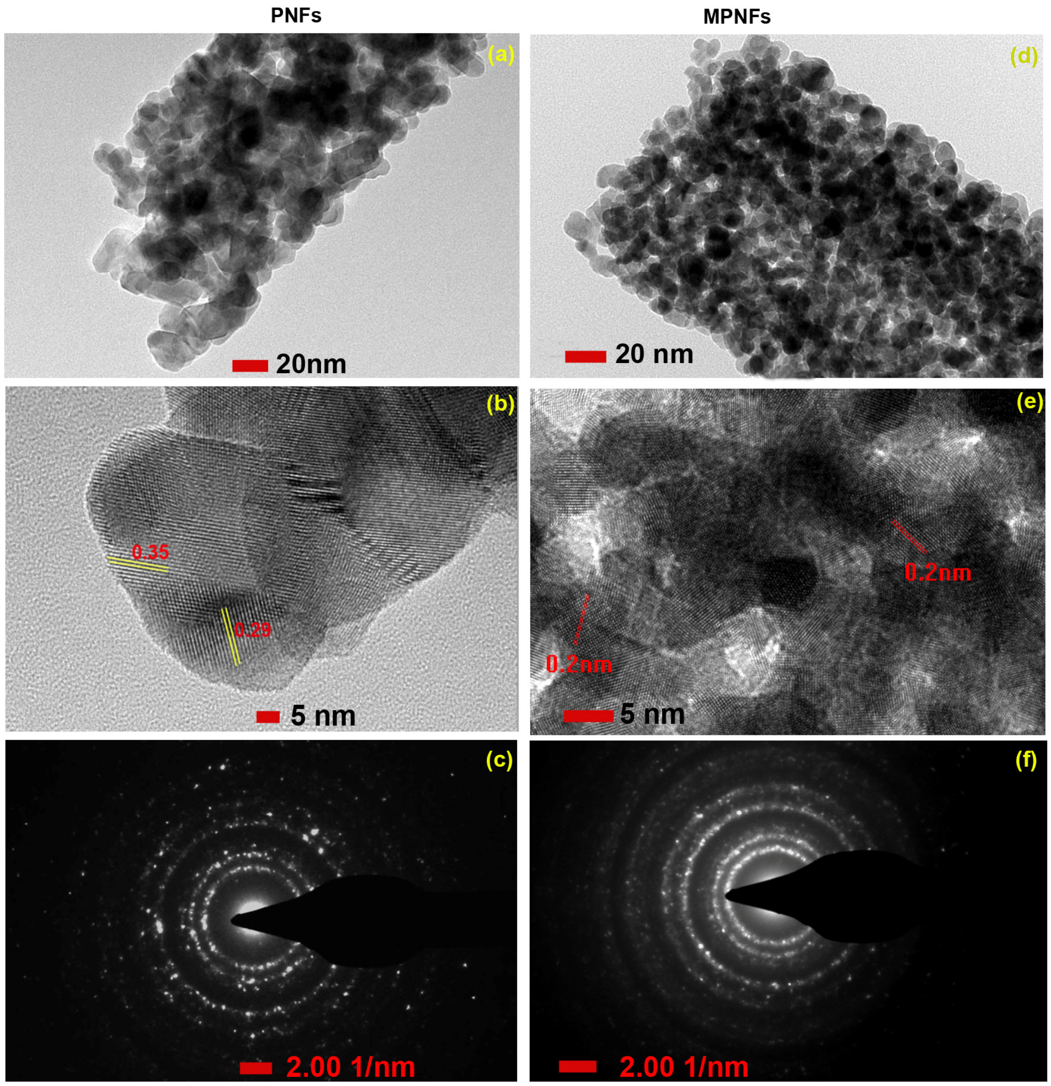

Fig. 3 TEM images of as synthesized SnO_2 PNFs and MPNFs (a, d) and (b, e) at low magnifications and high magnification, while (c, f) represent the selected area electron diffraction (SAED) pattern respectively.

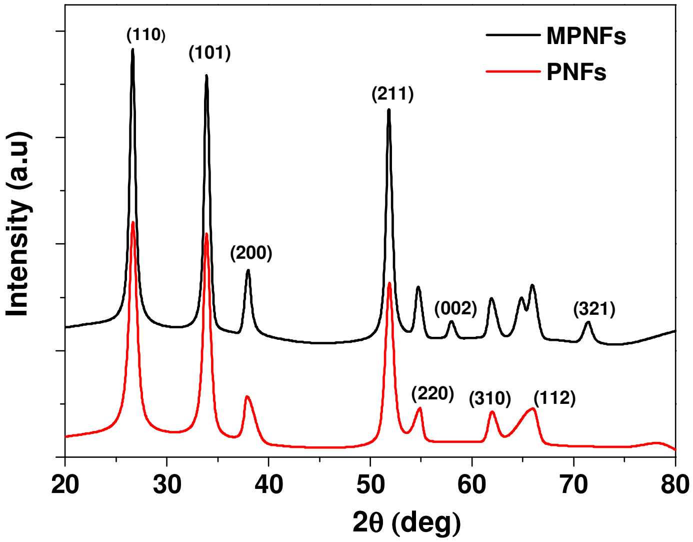

Fig. 4 XRD patterns of and PNFs and MPNFs.

3.3 Current Voltage (I-V) characteristics

To realize the effect of increased surface area in MPNFs, photoanodes were fabricated for DSCs. Fig. 5 is SEM images showing the cross-sectional view of the photoanodes fabricated using PNFs and MPNFs, respectively. Thickness of the films was 17± 0.5 µm. The PNFs and MPNFs retained their morphologies even after extensive mechanical agitation during the paste making procedure and subsequent thermal annealing. No agglomeration was found in the photoanode film; ensuring high porosity for efficient electrolyte penetration.[31]

The dye-loading on photoanodes was calculated by the desorption test. The calculated dye-loading of MPNFs is 3.38×10^{-7} mole cm^{-2} which is over 4 times larger than that of PNFs (0.83×10^{-7} mole cm^{-2}). The significantly enhanced dye-loading is attributed to the higher surface area of MPNFs (ESI†, FigureS3). A control electrode of TiO_2 was also fabricated using commercial P25 paste. The dye-loading of the P25-based electrode (7.02×10^{-7} mol/cm^2) is twice that of the MPNFs based electrodes. The current-voltage analysis of the DSCs is in Fig. 6 and the corresponding photovoltaic parameters are listed in the Table 2. As expected from high surface area in MPNFs, a high short circuit current density, J_{SC} = 18 mA cm^{-2} and PCE ~ 4.3% were obtained for the MPNFs DSCs while those for PNFs DSCs are less than its half (J_{SC} = 10 mA cm^{-2} and PCE ~2%). The V_{OC} in MPNFs DSCs showed an increment of 0.57 mV as a consequence of the enhanced J_{SC}. The fill factors (FF) of both devices remind practically same (0.47 in MPNFs and 0.45 in PNFs). As the thickness of both the electrodes is same, the presence of multichannels in MPNFs and their smaller grain size compared to PNFs, which resulted up to 8 times increased surface area and up to 5 times larger dye loading, is attributed to the higher J_{SC}.

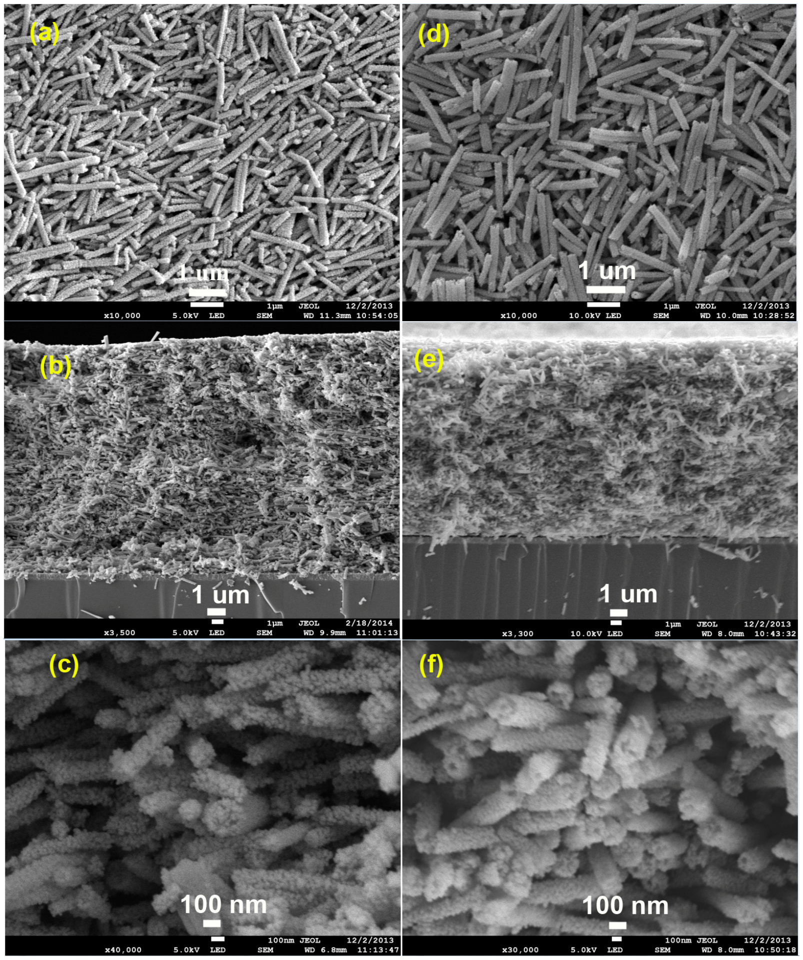

Fig. 5 (a,d) show the top views of the coated PNFs and MPNFs photoanodes whilst (b–e) and (c–f) demonstrate the cross sectional view at low and high magnification, respectively.

The low V_{OC} and FF are the main issues in SnO_2 based DSCs due to its lower conduction band edge which results in high electron recombination with the electrolyte species.[32] In order to suppress the charge recombination, we introduced a thin layer of TiO_2 onto the SnO_2 PNFs and MPNFs photoanodes by $TiCl_4$ treatment (the treated samples are named T-PNFs and T-MPNFs respectively).[33] The $TiCl_4$ treated photoelectrode showed remarkable increase in photovoltaic parameters (Fig. 6) as observed by others.[34] The V_{OC}, J_{SC}, and PCE in MPNFs DSCs increased from 0.51 to 0.66 V, 18 to 24 mA cm^{-2}, and 4.3% to 7.4%, respectively. The observed 30% increase in V_{OC} and 33% increase in J_{SC} resulted in ~80% increment in final PCE upon $TiCl_4$ treatment. Similar increase in photovoltaic parameters is observed for PNFs DSCs as shown in Table 2. For MPNFs DSCs. Our fabricated P25 DSCs showed PCE up to 7.6% (V_{OC}= 0.72V, J_{SC}=17.4, and FF= 0.61), which are comparable to the values reported for the chosen configuration and choice of dye and electrolyte.[27] The MPNFs DSCs have significantly larger J_{SC} and nearly similar PCE to that employed pure TiO_2 despite its significantly larger V_{OC} (10%) and FF (30%). To the best of our knowledge these are the highest PV parameters reported for SnO_2 based DSCs.

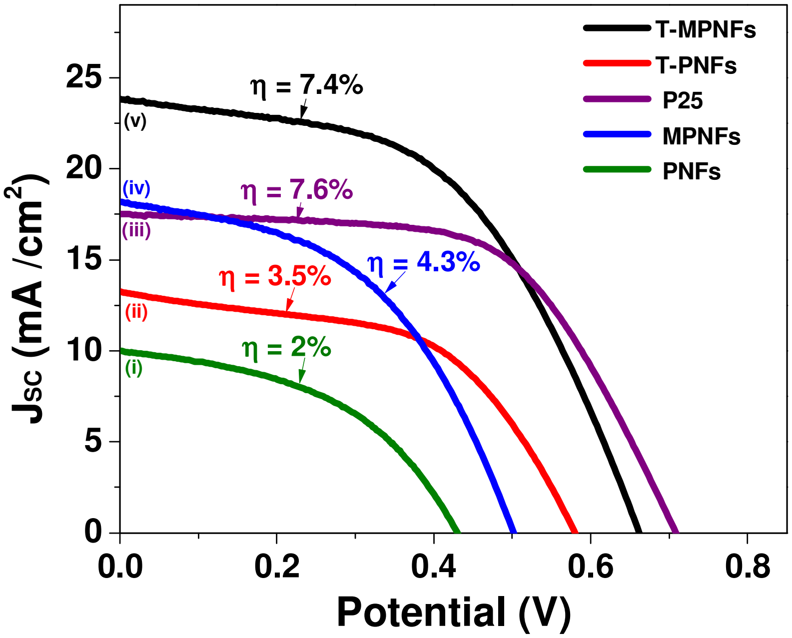

Fig. 6 Current density versus voltage (J–V) curves of (i) pure PNFs, (ii) pure MPNFs, (iii) P25, (iv) T-PNFs, and (v) T-MPNFs DSCs at AM 1.5G conditions.

Table 2 Photovoltaic parameters (J_{SC}, V_{OC}, FF and PCE) of (i) PNFs, (ii) MPNFs, (iii) P25, (iv) T-PNFs and (v) T-MPNFs DSCs at air mass 1.5G.

Device	J_{SC} (mA cm^{-2})	V_{OC} (V)	FF	PCE (%)	Specific surface area (m^{2}g^{-1})	Dye loading (×10^{-7} mole cm^{-2})
PNFs	10	0.44	0.45	2	10 – 12	0.83
MPNFs	18	0.51	0.47	4.3	78	3.38
P25	17.4	0.72	0.61	7.6	150	7.02
T-PNFs	13.5	0.57	0.45	3.5	--	--
T-MPNFs	23.7	0.66	0.47	7.4	--	--

Incident photon to current conversion efficiency (IPCE)

The I-V results were validated by measuring the incident photon to current conversion efficiency (IPCE) of the devices (Fig. 7a) and calculating the J_{SC} using the relation

$$IPCE(\%) = \frac{J_{SC}(mA/cm^2)}{P(mW/cm^2)} \times \frac{1240}{\lambda(nm)} \times 100\%. \qquad (1)$$

The integrated IPCE over the entire wavelength (λ) was used to calculate the J_{SC}. Fig. 7a shows the IPCE spectra of the devices. The calculated J_{SC} of the T-MPNFs, T-PNFs, and P25 DSCs were 20.5, 13, and 15.4 mA/cm^2, respectively, which match closely with their measured J_{SC} from the I-V measurements (Table 2). A significant increase in the IPCE of the T-MPNFs over the others was observed. The highest IPCE for T-MPNFs, T-PNFs, and P25 DSCs are ~83%, 57%, and 68%, respectively. The increased IPCE of the T-MPNFs DSCs over the T-PNFs could be attributed to its significantly larger dye-loading. However, its dye-loading is only half to that of P25 DSCs thereby implying that improved J_{SC} of the T-MPNFs results from both dye-loading and desirable charge transport characteristics. Furthermore, an enhanced light scattering in the case of both T-MPNFs and T-PNFs is noticed at wavelengths > 560 nm which is attributed to the bigger size of 1D tubular material than that of P25 particles. An improved charge transport in SnO_2 can be normally expected due to its many fold increased electron mobility compared to that of the TiO_2.

Open circuit voltage decay (OCVD) measurement

To prove improved charge transport in SnO_2 over TiO_2, we measured the electron lifetime (τ_n) from open circuit voltage decay (OCVD) measurements. The OCVD is a simple technique to investigate real-time recombination kinetics in DSCs by changing their equillibrium state from illuminated to dark.[35] The DSCs are kept under constant illumination which is then interupted. The decay in the V_{OC} is recorded as a function of time (ESI†, Figure S4) during relaxation. It is evident that the V_{OC} decay rate was significantly lower for T-MPNFs DSCs as compared to T-PNFs and P25 suggesting low recombination of photoexcited electrons. The τ_n is calculated by using the expression $\tau_n = -\frac{K_B T}{e}\left(\frac{dV_{OC}}{dt}\right)^{-1}$ where K_BT is thermal energy, e is the elementary charge and dV_{OC}/dt is the first order derivative of V_{OC}.[34] The T-MPNFs DSCs showed the highest τ_n; for example, at 0.3 V, T-MPNFs gave τ_n ~7 s whereas it is 2.3 and 1.47 sec for T-PNFs and P25 DSCs, respectively (Fig. 7b). Our calculated τ_n for P25 DSCs is similar to that obtained by Zaban *et al.*[34] i.e., (~20 ms – 1s) for a P25 nanoparticle based high efficiency DSCs. The high τ_n observed in SnO_2 can be attributed to their 1D morphology as well as improved charge mobility through it.

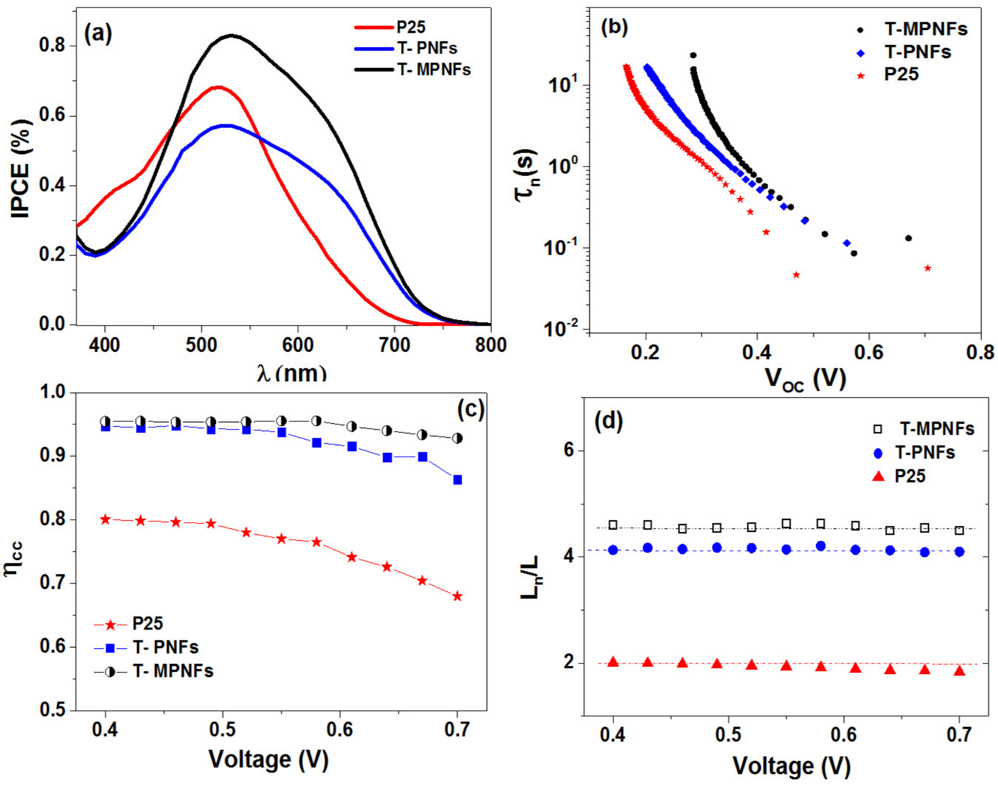

Fig. 7(a) Incident photon to current conversion efficiency (IPCE) curves of the three DSCs (T-PNFs, T-MPNFs and P25), (b) the τ_n calculated from OCVD data, (c) charge collection efficiency of the three DSCs (d) Electron diffusion length calculated using a well-known electrical equivalent model.

Collection efficiency and diffusion length

The collection efficiency of the devices were compared from τ_n and electron transit time τ_d by using the expression $\eta_{cc} = 1 \Big/ \left(1 + \left(\tau_d / \tau_n\right)\right)$.[36] As shown in Fig. 7c, the T-MPNFs DSCs showed ~21% increased charge collection than that of P25 and slightly increased charge collection than that of T-PNFs in photoanodes of similar thickness (17±0.5 μm). This increment is due to the fact that the diffusion length ($L_n = L\sqrt{R_{CT}/R_T}$), i.e., the distance travelled by electrons before recombination,[37,38] in T-MPNFs based photoanodes is 2 – 3 times higher than that of P25 (See ESI† for details on impedance analysis and L_n calculations, Figure S5 – S8). L_n, which is ~70 – 75 μm in T-MPNFs DSCs, ~65 – 70 μm in T-PNFs and ~30 – 35 μm in P25 DSCs (Fig. 7d), clearly estabilishes the effect of 1D nature of the tubular nanostructures. An enhanced τ_n and significantly higher L_n demonstrates the benifical effects when 1D nanomaterial MPNFs architecture are employed as a photoanode material.

Conclusions

In conclusion, we have fabricated various one-dimensional nano-morphologies of SnO_2 such as nanowires, nanofibers, and multiporous nanofibers via electrospinning by controlling the tin precursor concentration. The multichannel nanotubes possessed the highest surface area among them with superior charge transport characteristics. The MPNFs excelled conventional nanofibers and nanowires when employed as a photoanode in DSCs; significantly higher short circuit current was achieved in MPNFs DSCs compared to the conventional devices employed commercial TiO_2 paste. The MPNFs enabled >80% charge collection (45% higher than spherical P25 TiO_2 particles) and also demonstrated ~3 times longer electron lifetime and electron diffusion length. Owing to the scalability of the electrospinning technique, desirable device characteristics, and huge commercial potential of SnO_2 nanostructures, the present materials are expected to be utilized in commercial devices.

Acknowledgements:

The authors acknowledge the research grant from Malaysian Technological University Network (MTUN) Centre of Excellence (MTUN-CoE) program on nanowire solar cells.

†Electronic Supplementary Information Available: S1 – SEM images of the as-spun polymeric nanofibers with varying tin precursor concentration and their XRD patterns in S2; S3 – results of dye-loading test; S4 – Measured OCVD curves; S5 – S8: extraction of charge transport parameters). These documents can be freely available through the internet via http://rsc.org.

References

1. A. P. Alivisatos, Science, 1996, **271**, 933-937.
2. C. Burda, X. Chen, R. Narayanan and M. A. El-Sayed, Chem. Rev.,2005, **105**, 1025-1102.
3. J. Hu, T. W. Odom and C. M. Lieber, Acc. Chem. Res., 1999, **32**, 435-445 .
4. Y. Xia, P. Yang, Y. Sun, Y. Wu, B. Mayers, B. Gates, Y. Yin, F. Kim and H. Yan, Adv. Mater., 2003, **15**, 353-389 .
5. G. K. Mor, O. K. Varghese, M. Paulose, K. Shankar and C. A. Grimes, Sol. Energy Mater. Sol. Cells, 2006, **90**, 2011-2075.
6. J. Wu, Z. Tang, Y. Huang, M. Huang, H. Yu and J. Lin, J. Power Sources, 2014, **257**, 84-89.
7. D. Li and Y. Xia, Adv. Mater., 2004, **16**, 1151-1170.
8. R. Ramaseshan, S. Sundarrajan, R. Jose and S. Ramakrishna, J. App. Phys., 2007, **102**, 111101.
9. C. J. Luo, S. D. Stoyanov, E. Stride, E. Pelan and M. Edirisinghe, Chem. Soc. Rev., 2012, **41** , 4708-4735.
10. S. Ramakrishna, R. Jose, P. S. Archana, A. S. Nair, R. Balamurugan, J. Venugopal and W. E. Teo, J.Mater. Sci., 2010, **45**, 6283-6312.
11. D. Li and Y. Xia, Nano Lett., 2004, **4**, 933-938.

12. X. L. Xie, Y. W. Mai and X. P. Zhou, Mater. Sci. Eng. R-Rep., 2005, **49**, 89-112.

13. E. N. Kumar, R. Jose, P. S. Archana, C. Vijila, M. M. Yusoff and S. Ramakrishna, En. & Env. Sci., 2012, **5**, 5401-5407.

14. R. Ostermann, D. Li, Y. Yin, J. T. McCann and Y. Xia, Nano Lett., 2006, **6**, 1297-1302.

15. J. Chen, C. Li, F. Xu, Y. Zhou, W. Lei, L. Sun and Y. Zhang, RSC Adv., 2012, **2**,7384-7387.

16. K. Wijeratne, J. Akilavasan, M. Thelakkat and J. Bandara, Electrochim. Acta, 2012, **72** ,192-198.

17. N. K. Elumalai, R. Jose, P. S. Archana, V. Chellappan and S. Ramakrishna, J. Phys. Chem. C, 2012, **116**, 22112-22120.

18. K. L. Chopra, S. Major and D. K. Pandya, Thin Solid Films, 1983, **102**, 1-46.

19. Y. Idota, T. Kubota, A. Matsufuji, Y. Maekawa and T. Miyasaka, Science, 1997, **276** ,1395-1397.

20. J. Yan, E. Khoo, A. Sumboja and P. S. Lee, ACS Nano, 2010, **4**, 4247-4255.

21. O. A. Fouad, G. Glaspell and M. S. El-Shall, Top. Catal., 2008, **47** , 84-96.

22. G. S. Kim, H. K. Seo, V. P. Godble, Y. S. Kim, O. B. Yang and H. S. Shin, Electrochem.Comm., 2006, **8**, 961-966.

23. S. Gubbala, V. Chakrapani, V. Kumar and M. K. Sunkara, Adv. Func. Mater., 2008, **18**, 2411-2418 .

24. P. Charoensirithavorn, Y. Ogomi, T. Sagawa, S. Hayase and S. Yoshikawa, J. Cryst. Growth, 2009, **311**, 757-759 .

25. R. Jose, V. Thavasi and S. Ramakrishna, J. Am. Ceram. Soc., 2009, **92** , 289-301.

26. G. Shang, J. Wu, M. Huang, J. Lin, Z. Lan, Y. Huang and L. Fan, The Journal of Physical Chemistry C, 2012, **116**, 20140-20145.

27. Z. Dong, H. Ren, C. M. Hessel, J. Wang, R. Yu, Q. Jin, M. Yang, Z. Hu, Y. Chen, Z. Tang, H. Zhao and D. Wang, Adv. Mater., 2014, **26**, 905-909 .

28. A. Fakharuddin, I. Ahmed, Z. Khalidin, M. M. Yusoff and R. Jose., App. Phy. Lett.,2014, **104**, 053905.

29. S. Ito, T. N. Murakami, P. Comte, P. Liska, C. Grätzel, M. K. Nazeeruddin and M. Grätzel, Thin Solid Films, 2008, **516**, 4613-4619.

30. J. Bisquert, J. Phys. Chem. B, 2002, **106**, 325-333.

31. Q. Zhang and G. Cao, Nano Today, 2011, **6**, 91-109.

32. Z. Li, Y. Zhou, R. Sun, Y. Xiong, H. Xie and Z. Zou, Chin. Sci. Bull.,2014, 1-13.

33. S. Ito, P. Liska, P. Comte, R. Charvet, P. Pechy, U. Bach, L. Schmidt-Mende, S. M. Zakeeruddin, A. Kay, M. K. Nazeeruddin and M. Grätzel, Chem. Comm., 2005, **2**, 4351-4353.

34. P. M. Sommeling, B. C. O'Regan, R. R. Haswell, H. J. P. Smit, N. J. Bakker, J. J. T. Smits, J. M. Kroon and J. A. M. Van Roosmalen, J. Phys. Chem. B, 2006, **110**, 19191-19197.

35. A. Zaban, M. Greenshtein and J. Bisquert, ChemPhysChem, 2003, **4** , 859-864.

36. N. Cai, S.-J. Moon, L. Cevey-Ha, T. Moehl, R. Humphry-Baker, P. Wang, S. M. Zakeeruddin and M. Grätzel, Nano Lett., 2011, **11**, 1452-1456.

37. Q. Wang, S. Ito, M. Grätzel, F. Fabregat-Santiago, I. Mora-Seró, J. Bisquert, T. Bessho and H. Imai, J. Phys. Chem. B, 2006, **110**, 25210-25221.

38. A. Fakharuddin, I. Ahmed, Z. Khalidin, M. M. Yusoff and R. Jose, J. App. Phys., 2014, **115**, 164509.

Table of Content Entry

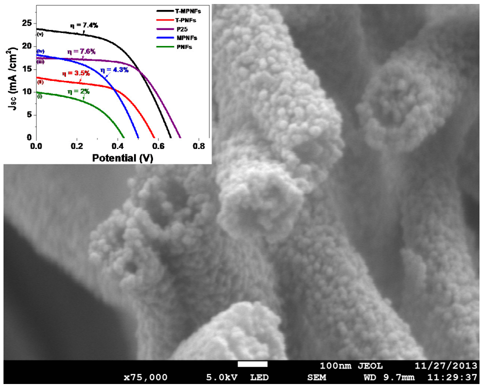

Tin oxide nanofibers developed by electrospinning by controlling the precursor concentration gave the highest photoconversion efficiency in dye-sensitized solar cells